TiO2 Nanotubes for Solar Water Splitting: Vacuum Annealing and Zr Doping Enhance Water Oxidation Kinetics

Maged N. Shaddad,[†,§] Drialys Cardenas-Morcoso,[‡,§] Miguel García-Tecedor,[‡] Francisco Fabregat-Santiago,[‡] Juan Bisquert,[‡] Abdullah M. Al-Mayouf,*,[†] and Sixto Gimenez*,[‡]

[†]Electrochemical Sciences Research Chair (ESRC), Department of Chemistry, Science College, King Saud University, Riyadh 11451, Saudi Arabia

[‡]Institute of Advanced Materials (INAM), Universitat Jaume I, 12006 Castelló, Spain

S Supporting Information

ABSTRACT: Herein, we report the cooperative effect of Zr doping and vacuum annealing on the carrier dynamics and interfacial kinetics of anodized TiO_2 nanotubes for light-driven water oxidation. After evaluation of different Zr loads and different annealing conditions, it was found that both Zr doping and vacuum annealing lead to a significantly enhanced light harvesting efficiency and photoelectrochemical performance. The substitution of Zr^{4+} by Ti^{4+} species leads to a higher density of surface defects such as oxygen vacancies, facilitating electron trapping on Zr^{4+}, which reduced the charge recombination and hence boosted the charge transfer kinetics. More importantly, vacuum annealing promoted the presence of surface defects. Furthermore, the mechanistic study through impedance spectroscopy revealed that both charge transfer and surface conductivity are significantly enhanced due the presence of an oxygen-deficient TiO_2 surface. These results represent an important step forward in the optimization of nanostructured TiO_2-based photoelectrodes, with high potential in photocatalytic applications, including solar fuel production.
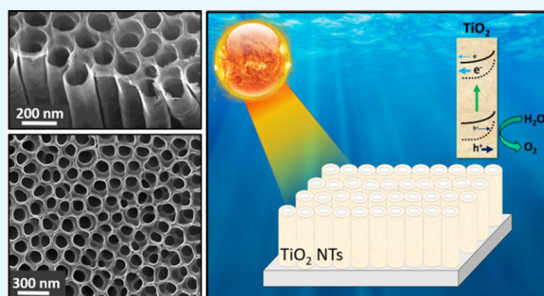
INTRODUCTION

One-dimensional nanostructures have attracted significant interest in the last years as advanced platforms for energy conversion and storage,[1,2] catalysis,[3] and sensing.[4] The ordered material architecture offers multiple advantages in terms of (i) unidirectional transport pathways uninterrupted by interparticle connections, (ii) the possibility to form surface electrical fields able to reduce recombination by confining the injected electrons to the central zone of the tubes, and (iii) improved penetration of the liquid/gas into the pores compared to disordered architectures, which is beneficial for photoelectrochemical and catalytic applications.[5] Furthermore, the size reduction to the nanometer scale leads to a higher surface-to-volume ratio, which can be beneficial for applications involving surfaces as catalytic and (photo)electrochemical applications.[6]

Several metal-oxide nanowire and nanotube architectures deposited on a conducting substrate for different applications have been reported, with most studies focusing on titanium dioxide (TiO_2) not only for its promising functional properties but also as a relevant model for mechanistic studies.[7−9] Consequently, several strategies have been explored to enhance the optoelectronic properties of TiO_2 (e.g., light harvesting, conductivity, charge transfer kinetics, recombination kinetics) aiming at boosting its performance for a particular application. For example, doping with C, N, and S atoms has showed enhanced optical absorption of TiO_2 by decreasing the band gap.[4,10,11] Heat treatment under reductive conditions (vacuum or H_2) has been reported as a successful method to increase the donor density concentration of TiO_2 through the introduction of a high density of oxygen vacancies, serving as electron donors.[4,11] Mechanistic studies have shown that the improved electrical properties of oxygen-deficient TiO_2 synthesized under reducing conditions are related to the effective suppression of carrier recombination coupled to enhanced charge separation.[12] Consistently, bulk and surface conductivities in TiO_2 nanotubes significantly increase due to the presence of oxygen-deficient TiO_2 nanolayers.[13] Indeed, hydrogenated TiO_2 also called black titania has resulted in a highly successful strategy to extend the optical absorption of this material to near infrared, significantly enhancing its optoelectronic and catalytic properties.[14,15]

On the other hand, homovalent doping of TiO_2 with Zr also yields enhanced performance, as widely documented in the literature. It was found that Zr incorporation into TiO_2 layers improved the performance in hybrid perovskite solar cells leading to longer carrier lifetimes and higher charge carrier densities, which have been ascribed to reduced defect sites in the bulk or at the interfaces of the perovskite.[16] Similar surface passivation effects on TiO_2 have been attributed to ZrO_2 nanolayers, in high-efficiency organic[17] and dye-sensitized
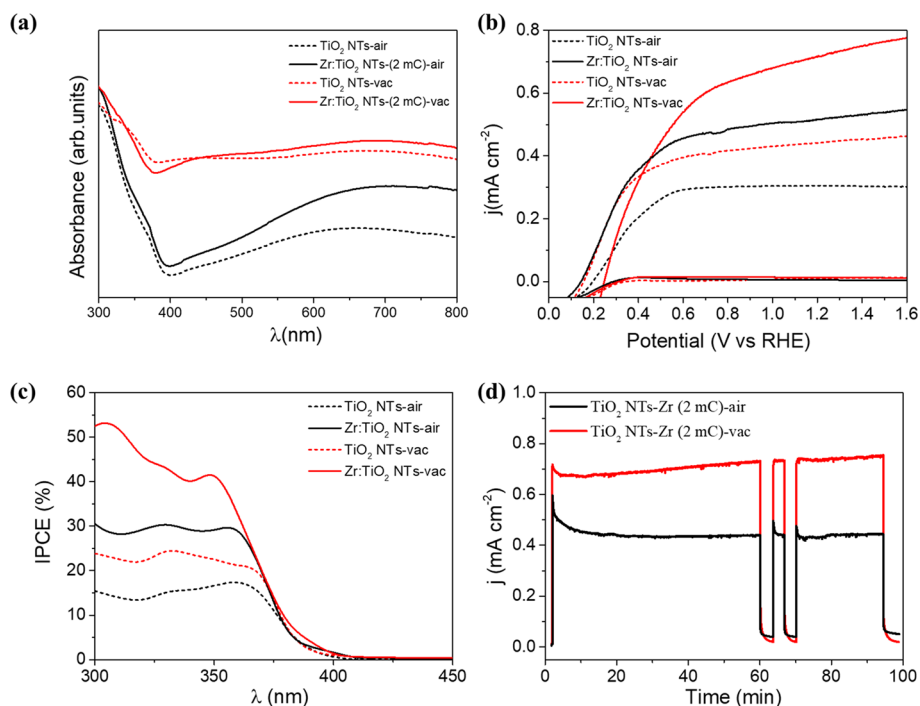
Figure 1. Optical and photoelectrochemical performances of bare and Zr-doped TiO$_2$ NTs, thermally treated under air or vacuum atmosphere: (a) absorbance spectra, (b) photocurrents for water oxidation (J−V curves in dark conditions are also shown for comparison), and (c) incident photon to current efficiency (IPCE) and (d) chronoamperiometric tests at 1.23 V vs RHE to evaluate the stability of the electrodes.
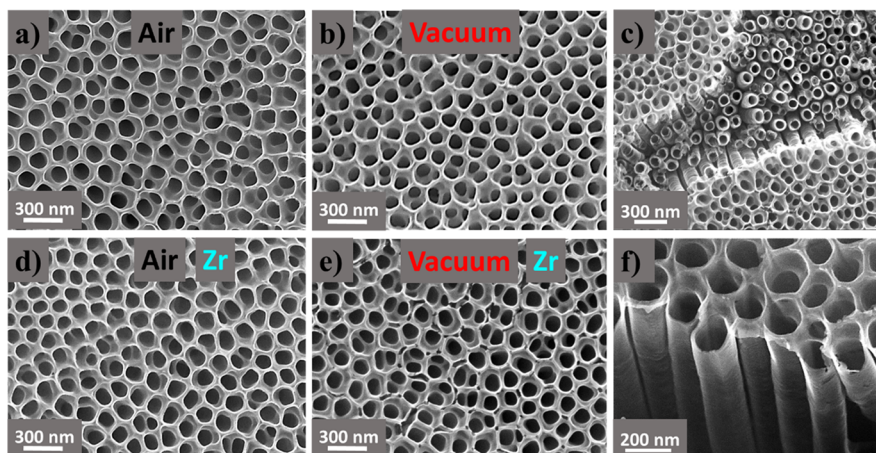

Figure 2. Zenithal SEM images of TiO$_2$ nanotubes synthesized with different thermal treatments under (a) air and (b) vacuum and with Zr addition under (d) air and (e) vacuum. (c,f) Illustration of the tubular morphology from a representative region of the vacuum-annealed Zr:TiO$_2$ NTs.

solid-state photovoltaic devices.[6] ZrO$_2$ coatings on TiO$_2$ also enhance optical scattering, which is beneficial for light harvesting increasing the optical pathway.[18]

In the present study, we report the combined effect of Zr incorporation and vacuum annealing on the photoelectrochemical properties of TiO$_2$ nanotubes for light-driven water oxidation. We have found that both Zr addition and vacuum annealing lead to the creation of surface oxygen vacancies, which produce optical scattering and consequently slightly enhanced light harvesting efficiency and more relevantly induce surface stress and an anodic band shift, both beneficial effects for enhanced photo-electrocatalytic activity of the TiO$_2$ nanotubes toward water oxidation.

■ RESULTS AND DISCUSSION

The combined effects of both Zr-doping and vacuum-annealing treatment on the optical and photoelectrochemical properties of TiO$_2$ nanotubes are shown in Figure 1. The onset wavelength at 400 nm observed in the absorbance measurement in Figure 1a perfectly agrees with the direct band gap of anatase TiO$_2$. It is worthy to note that both vacuum annealing and Zr addition produce a higher sub-band gap absorbance signal (at wavelengths >400 nm). We have ascribed this signal to optical scattering, as previously reported for ZrO$_2$-decorated TiO$_2$ nanoparticles.[19] The precise values of the band gap were determined from the Tauc plots for direct optical transitions, as shown in Figure S1. The measured photocurrents, which we ascribe to oxygen evolution,[20,21] are significantly higher upon

Zr doping in both vacuum and air atmosphere. Additionally, the highest performance is obtained under vacuum annealing conditions (Figure 1b). The spectral signature of the photocurrent was determined by incident photon to current efficiency (IPCE), as shown in Figure 1c. Furthermore, the integrated photocurrents, shown in Table S1, are consistent with those reported in Figure 1b at 1.23 V versus RHE. The stability of the different photoelectrodes was assessed by chronoamperometric experiments at 1.23 V_{RHE}, as depicted in Figure 1d. The measurements show stable photocurrents (for 100 min) of around 0.7 mA cm^{-2} for vacuum-annealed samples and 0.45 mA cm^{-2} for air-annealed samples. Note that the anodic transients observed in the air-annealed samples after switching the light on are suppressed for the vacuum-annealed ones, suggesting a significant reduction of surface recombination.

In order to explain the origin of the increased performance after optimal Zr doping and annealing under vacuum conditions, a detailed optical, morphological, and structural characterization was carried out. First, the optimized Zr content on the TiO$_2$ nanotubes was determined after testing different Zr loads by varying the total applied charge during the cathodic electrodeposition process (see the Experimental Section for the detailed procedure). The results are summarized in Figure S2a, finding that the optimized electrodeposited charge corresponds to 2 mC. Consequently, throughout the rest of the manuscript, unless otherwise specified, the optimized Zr-doped TiO$_2$ nanotube photoelectrodes are labeled as Zr:TiO$_2$ NTs. Upon different Zr additions, the highest sub-band gap absorbance (mainly related to optical scattering) takes place for the optimized electrodeposited charge (Supporting Information, Figure S2b), which is beneficial for light harvesting due to the enhanced optical path in the nanotube film. This effect can partially account for the slight increase in the absorbance in the 300−400 nm region and the photocurrent and IPCEs shown in Figure 1c.

Figure 2 summarizes the morphological analysis of the TiO$_2$ nanotubes with and without the optimal Zr addition for the two different thermal treatments (air and vacuum). The characteristic parameters of the different nanotubes are 150 nm tube diameter, 20 nm wall thickness, and around 1 μm tube length. The surface density estimated by image analysis was ~150 tubes/μm^2. In all cases, the composition determined by EDS analysis perfectly agrees with stoichiometric TiO$_2$ (Supporting Information, Figure S3 and Table S2). The amount of Zr present in the samples is under the detection limit of the EDS technique, and no Zr could be identified in any of the tested Zr:TiO$_2$ NT samples with this technique. It is noted that practically identical microstructures are obtained for the different thermal treatments, and consequently, the different observed photocurrents in Figure 1b are not related to morphological differences between the tested samples.

The crystalline structure of the materials was determined by XRD (Supporting Information, Figure S4 and Table S3). All tested TiO$_2$ samples heat-treated in the two different atmospheres (air and vacuum) and independently of the Zr addition exhibited the pure anatase phase (JCPDS card no. 21-1272) without any trace of secondary phases. The diffraction peak associated with the (101) planes is dominant in both undoped and Zr-doped samples, as reported for other titania nanotubes.[22] Note that, due to the small amount of Zr, the observation of peak shifts or broadening effects in the XRD diffractograms is not straightforward. On the other hand,

higher-resolution structural information was obtained with TEM analysis. Again, independent of the Zr addition or the atmosphere during the heat treatment, the nanotubes presented a very similar structure (Supporting Information, Figure S5a). Representative selected area electron diffraction (SAED) patterns shown in Figure S5b clearly evidenced that, in all cases, the *hkl* interplanar distances corresponded to pure anatase,[23] in good agreement with the XRD results. Consistently, EDS analyses carried out in the TEM chamber confirmed the stoichiometry of the samples as TiO$_2$ (Supporting Information, Figure S6).

The negligible microstructural differences between bare and treated TiO$_2$ nanotubes cannot account for the remarkable differences in performance observed in Figure 1. This suggests that the effect of both heat treatment atmosphere and Zr doping should be confined to the surface of the nanotubes. Consequently, a detailed surface characterization of the TiO$_2$ nanotubes in all tested conditions was carried out by X-ray photoelectron spectroscopy (XPS), as shown in Figure 3 and
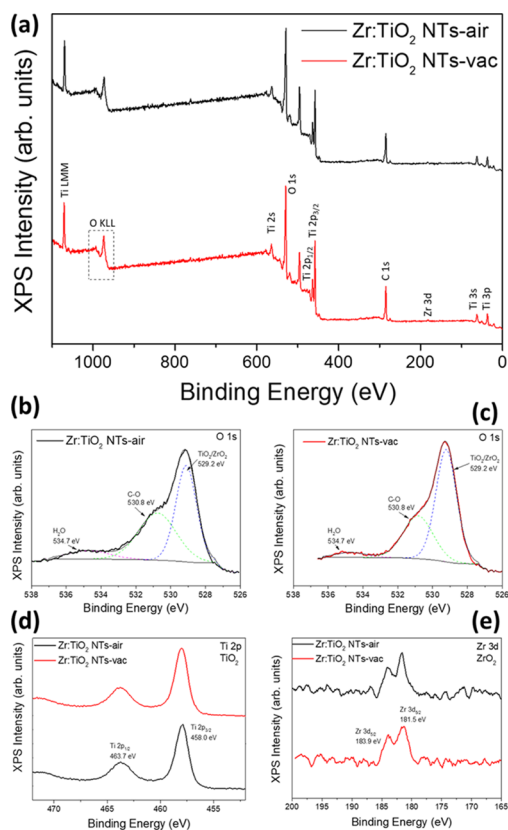

Figure 3. (a) XPS survey of Zr-doped TiO$_2$ nanotubes under air and vacuum atmospheres. XPS results on O 1s orbital for Zr:TiO$_2$ NTs under (b) air and (c) vacuum. XPS results on analyzed samples corresponding to (d) Ti 2p and (e) Zr 3d orbitals.

Table S4. The survey spectrum reveals the presence of Ti, O, and Zr. The shoulder located at 429 eV, inside the complex band associated with the O 1s orbital, confirms the presence of O^{-2} ions, bonded with Ti^{4+} or Zr^{4+} to form the associated oxide compounds (Figure 3b,c). Indeed, it has been reported that immediate oxidation of Zr to ZrO$_2$ takes place when electrodeposited Zr from DMSO solution is in contact with air.[24] The peaks associated with Ti 2p$_{1/2}$ and 2p$_{3/2}$, located at 464 and 458 eV, respectively, confirm the 4+ state of Ti
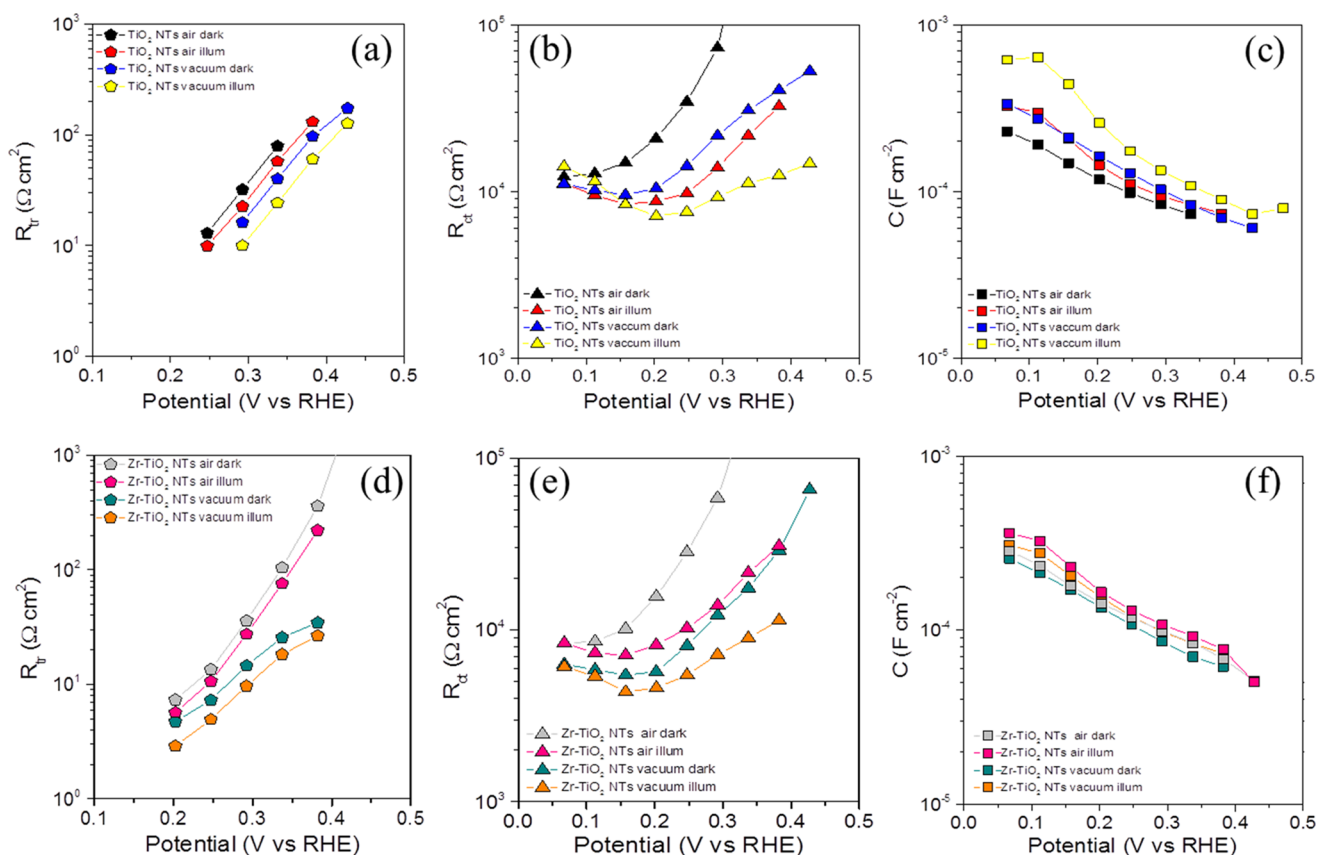
Figure 4. Fitted parameters from the EIS analysis in the dark and under illumination: (a−c) transport resistance (R_{tr}), charge transfer resistance (R_{ct}), and capacitance (C), respectively, in bare TiO_2 NTs; (d−f) same in Zr:TiO_2 NTs. The lines are guides for the eye.

associated with TiO_2, as shown in Figure 3d. The presence of Zr at the surface of the doped samples is also evidenced by the presence of two peaks located at 184 (Zr $3d_{3/2}$) and 181 eV (Zr $3d_{5/2}$) confirming the 4+ state characteristic of ZrO_2 (Figure 3e). The amount of Zr was estimated as ∼0.3 at. % for all the Zr:TiO_2 analyzed samples, which is at the detection limit of the XPS instrument.[25] The fact that Zr was bonded to oxygen in the 4+ state clearly supports the partial substitution of Ti^{4+} by Zr^{4+} ions. Indeed, the surface substitution of Zr^{4+} by Ti^{4+} species is expected due to their similar ionic radii (0.72 and 0.61 Å, respectively).[26,27] Some authors have reported that, even if the ionic radius of Zr^{4+} is slightly higher than that of Ti^{4+}, Zr can still be easily accommodated into the TiO_2 crystalline lattice.[28] To alleviate the strain induced by the size difference between the two ions, the lattice oxygen, particularly surface oxygen, escapes from the lattice and leads to the formation of a surface hole trap. This effect has been reported to improve the photocatalytic performance of TiO_2 nanotubes,[28] in good agreement with the results of Figure 1b. Furthermore, the incorporation of a higher amount of the substitutional dopant (Zr) can induce excessive strain in the crystal lattice of the host, favoring the presence of structural defects, which can also act as recombination centers.[19] Then these structural defects induced by excessive strain explain the observed decrease in performance upon increasing the loaded charge of Zr beyond 2 mC on the TiO_2 nanotubes (Supporting Information, Figure S2). On the other hand, compared to pristine TiO_2 samples, the higher density of surface defects with Zr addition is consistent with the increased optical scattering shown in Figure 1a. Indeed, the effect of the optimal

Zr doping favoring the creation of defects in TiO_2 has been reported to facilitate electron trapping on Zr^{4+} rather than on Ti^{4+} leading to reduced charge recombination and subsequently boosting charge transfer kinetics and hence performance.[19,29]

Regarding the use of reductive atmospheres (vacuum annealing in the present study), an increase in the water splitting performance for anatase TiO_2 nanotubes has been already reported under hydrogen annealing.[11,12] This enhancement of performance has been associated with the creation of oxygen vacancies and Ti^{3+} species that acts as electron donor species.[11,30] Compared to air-annealed samples, a slight decrease in the oxygen concentration was detected in the vacuum-annealed samples by XPS (Supporting Information, Table S4). This decrease of oxygen can be attributed to a higher concentration of oxygen-deficient-related surface defects, which enhance the water oxidation performance (Figure 1b). Previous studies demonstrate that oxygen vacancies are more likely formed at the surface, rather than within the bulk of TiO_2, as suggested by our structural, electrical, and surface characterization, but these defects are not so mobile as the Ti^{3+} species, which can migrate via interstitial positions.[31] The optical scattering and improved absorbance observed in Figure 1a for vacuum-annealed samples are also in good agreement with previous reports where the use of reductive atmospheres leads to the presence of defects (O_2^- vacancies, F^+ color centers, and Ti^{3+} species are the most common defects in the (101) planes of TiO_2), which can enhance light absorption.[22]
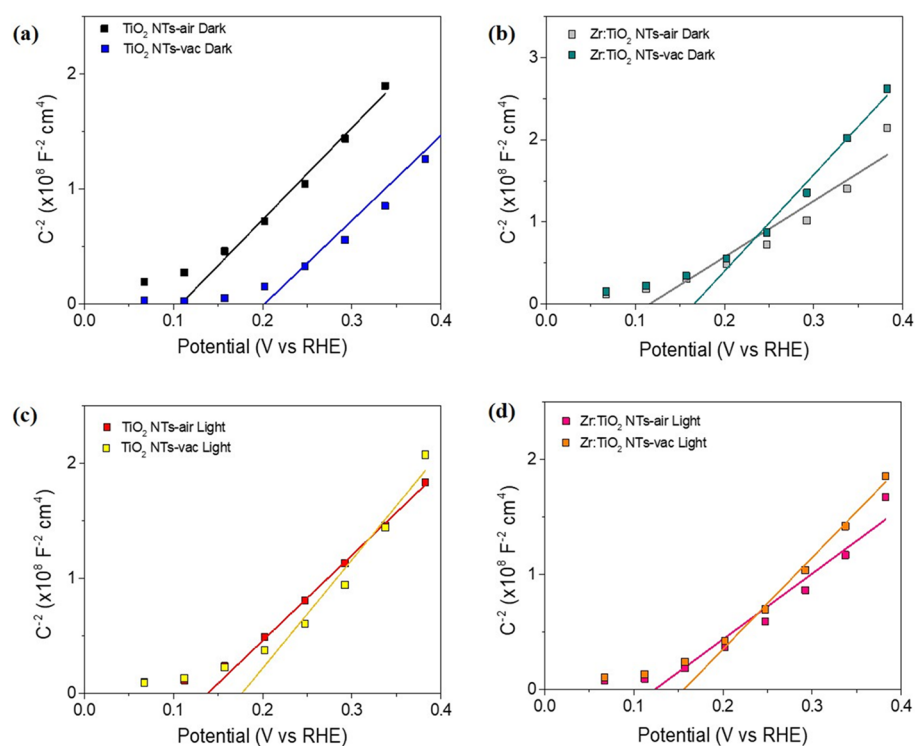
Figure 5. Mott−Schottky plots of the capacitance of bare and Zr-doped TiO$_2$ nanotubes thermally treated in air and vacuum: (a,b) in the dark; (c,d) under illumination.

Further mechanistic insights were extracted from impedance spectroscopy measurements in the dark and under illumination on Zr:TiO$_2$ NTs after thermal treatment in air or vacuum. The raw data were fitted to an equivalent circuit classically used in nanostructured TiO$_2$ architectures where transport and charge transfer/recombination are coupled (Supporting Information, Figure S7). The outcome of this fitting procedure led to the determination of transport resistance R_{tr} (linked to electron conductivity), charge transfer resistance R_{ct} (related to water oxidation catalysis), and capacitance C (related to the charge storage mechanism). These values as a function of the applied potential are presented in the Figure 4. The capacitances show an anodic shift under vacuum annealing and Zr addition, which can be related to hole accumulation at the photoelectrode surface. Furthermore, the charge transfer resistance R_{ct} (Figure 4b,e) shows lower values for the vacuum-annealed Zr:TiO$_2$ NTs, indicating the enhanced water oxidation kinetics at the surface of the electrode, consistent with the enhanced catalytic activity of slightly stressed surface, due to the presence of surface defects.[28] On the other hand, R_{tr} (Figure 4a,d) decreases in the vacuum-annealed Zr:TiO$_2$ NTs, supporting that surface conductivity is significantly enhanced due to the presence of an oxygen-deficient TiO$_2$ surface, in good agreement with a previous report.[24] From the obtained R_{ct} and R_{tr} values, the diffusion length was also calculated for the analyzed samples and for all the cases was in the order of several tens of micrometers (Supporting Information, Figure S8). Hence, the carrier diffusion is not limiting the performance of our TiO$_2$ nanotubes for water oxidation. Therefore, the main responsible factors for the enhanced performance are enhanced kinetics, although surface transport is also improved under the cooperative action of Zr addition and vacuum annealing. It is worthy to note that the series resistance (R_s) related to the resistance of the substrate and the contacts is

systematically below 12 Ω in all cases due to the high conductivity of the metallic Ti substrate (Supporting Information, Figure S9).

Moreover, at the tested potentials, the photoelectrode is driven to reverse polarization, and the obtained capacitance (Figure 4c,f) shows the classical Mott−Schottky behavior (vide infra in Figure 5) reflecting a large donor density of the n-type TiO$_2$ nanotubes (Supporting Information, Table S5).[5] The flat band potential is anodically shifted upon vacuum annealing (Figure 5), which is consistent with the anodic shift of the photocurrent onset potential for the optimal combination in Figure 1b, due to the higher thermodynamic driving force for water oxidation as result of the hole accumulation at the photoelectrode surface, and nicely explains the enhanced water oxidation performance as a result of the cooperative effect of both vacuum annealing and optimal Zr addition. However, in contrast to previous studies where the use of reductive atmospheres led to increased donor density,[4,11] this quantity does not significantly change in all tested conditions (Supporting Information, Table S5), confirming that the increased density of oxygen vacancies measured by XPS is not translated into the TiO$_2$ bulk. The thickness of the space charge layer (w) was also calculated for all tested TiO$_2$ nanotubes (Supporting Information, Figure S10), and the obtained results are in the range of 1 nm, validating that the above described morphology can accommodate such a band bending. We note that a specific Mott−Schottky equation for a tubular structure was not used in the present study.[32] However, the present results can be qualitatively valid to explain the observed performance.

■ CONCLUSIONS

In summary, we have demonstrated that the cooperative effects of Zr incorporation and vacuum annealing are related to

enhanced surface activity of the TiO_2 nanotubes, which results in improved water oxidation performance, although the quantitative contribution of vacuum annealing is more important than Zr addition. Both doping and vacuum annealing lead to a slightly stressed surface and consequently to a catalytically more active TiO_2 surface, concomitant to the creation of surface defects (oxygen vacancies), which enhance transport. Vacuum annealing produces an anodic band shift, highly beneficial for the accumulation of surface holes needed for water oxidation. Furthermore, Zr doping and vacuum annealing induce optical scattering, enhancing the optical pathway of incoming light and slightly increasing light harvesting efficiency of the TiO_2 nanotube films. These results contribute to the understanding and design of efficient photo-electrochemical cells for solar fuel production.

■ EXPERIMENTAL SECTION

Synthesis of TiO_2 Nanotube Electrodes. TiO_2 NT arrays were synthesized by a two-step electrochemical anodization of Ti foil at room temperature. First, a 0.25 mm thick Ti foil (>99.5% purity, Alfa Aesar) was cleaned with acetone and deionized (DI) water in an ultrasonic bath for 30 min. Then the foil was subjected to potentiostatic anodization for 30 min in a two-electrode electrochemical cell with Pt foil as the counter electrode. A constant voltage of 60 V was employed for the anodization, and the electrolyte used was 0.12 M NH_4F (Sigma-Aldrich) in a 5:100 (w/w) mixture of DI water and ethylene glycol (EG). The Ti foil was taken out and was ultrasonically cleaned in DI water for few seconds for the next round of potentiostatic anodization under identical conditions, but now, the time was 3 h. The anodized Ti foil was rinsed with DI water several times and annealed in air at 450 °C for 2 h with a ramp rate of 2 °C min^{-1} to obtain crystalline TiO_2 nanotubes on the Ti foil. Alternatively, TiO_2 nanotubes with different Zr additions were obtained by electrodeposition using an electrodeposition bath composed of 5 mM zirconium(IV) acetylacetonate ($C_{20}H_{28}O_8Zr$, Sigma-Aldrich) in dimethyl sulfoxide (DMSO). The electrodeposition was carried out in a three-electrode cell consisting of a TiO_2 nanotube (as anodized) working electrode, a Pt counter electrode, and a Ag/AgCl (3 M KCl) reference electrode. Cathodic deposition was performed potentiostatically at −2.0 V versus Ag/AgCl by varying the total deposited charge (2, 5, 10, 15, and 20 mC). The film was then heated at 450 °C for 2 h in air (ramping rate = 2.0 °C min^{-1}). The TiO_2 NT arrays (bare and Zr-doped) were annealed a second time under vacuum conditions or in an air atmosphere for comparison.

Structural, Optical, and Photoelectrochemical Characterization. Morphological and compositional characterization of the electrodes was studied by field-emission scanning electron microscopy (FE-SEM) with a JSM-7000F JEOL FEG-SEM system (Tokyo, Japan) equipped with an INCA 400 Oxford EDS analyzer (Oxford, U.K.) operating at 15 kV and a JEM-2100 JEOL transmission electron microscope (TEM) operating at 200 kV. Prior to the FE-SEM experiment, the samples were sputtered with a 2 nm thick layer of Pt. X-ray diffraction spectra were recorded using a Rigaku Miniflex 600, (Rigaku Corporation, Tokyo, Japan) with Cu Kα radiation (λ = 1.5418 Å) at a scan speed of 3° min^{-1}. Surface analysis was carried out by X-ray photoelectron spectroscopy (XPS) using a Specs SAGE 150 instrument. The analyses were performed using nonmonochrome Al Kα irradiation (1486.6 eV) at 20 mA and 13 kV, a constant energy pass of 75 eV for overall

analysis, 30 eV for analysis in the specific binding energy ranges of each element, and a measurement area of 1×1 mm^2. The pressure in the analysis chamber was 8×10^{-9} hPa. The data were evaluated using CasaXPS software. The energy corrections of the spectra were performed considering a reference value of C 1s from the organic matter at 284.8 eV. Optical properties of the prepared films were also determined through UV−vis spectroscopy of the electrodes recorded with a Cary 300 Bio spectrometer. The absorbance (A) was estimated from transmittance (T) and diffuse reflectance (R) measurements as $A = -\log(T + R)$. The direct optical band gap was estimated by the Tauc plot as $(h\upsilon\alpha)^{1/n} = A(h\upsilon - E_g)$, where $n = 1/2$ for direct transitions.

The photoelectrochemical performance of the electrodes was evaluated by linear sweep voltammetry in the dark and under illumination in a three-electrode cell consisting of a working electrode, a Ag/AgCl (3 M KCl) reference electrode, a Pt wire as a counter electrode, and 1 M NaOH (pH 13.6) electrolyte at a scan rate of 5 mV s^{-1}. The electrode area was 0.12 cm^2 defined by an epoxy frame. Alternatively, a 0.1 M Na_2SO_3 solution was added to the electrolyte as a hole scavenger. The measurements were carried out by using an Autolab potentiostat/galvanostat PGSTAT302, and a 300 W Xe lamp was used for those experiments under illumination conditions. The light intensity was adjusted to 100 mW/cm^2 using a thermopile, and illumination was carried out through the electrolyte. All the potentials were referred to the reversible hydrogen electrode (RHE) through the Nernst equation: $V_{RHE} = V_{Ag/AgCl} + V^0_{Ag/AgCl} + 0.059$pH. Incident photon to current efficiency (IPCE) measurements were performed with a 150 W Xe lamp coupled with a monochromator and an optical power meter. The photocurrent was measured at 1.23 V versus RHE, with a 10 nm spectral step. IPCE was calculated through the expression IPCE (%) $= \frac{I_{ph}(A)}{P(W)} \times \frac{1239.8}{\lambda\,(nm)} \times 100$, where I_{ph} is the photocurrent measured at a wavelength λ and P is the power of monochromatic light at the same wavelength. Electrochemical impedance spectroscopy (EIS) measurements were performed between 50 mHz and 1 MHz with 20 mV amplitude perturbation, with a step potential of 64 mV in the anodic direction. The EIS data were analyzed with ZView software (Scribner Associates). With the extracted capacitance values from EIS, Mott−Schottky analysis was carried out using the expression $\frac{1}{C_{SC}^2} = \frac{2}{\varepsilon_0\varepsilon_r e N_D A^2}\left(\phi_{SC} - \frac{kT}{e}\right)$, where C_{SC} represents depletion capacitance, $\phi_{SC} = V - V_{FB}$ is the voltage drop at the space charge region, V is the applied voltage, V_{FB} is the flat band potential, N_D is the donor density, e is the elementary charge, ε_0 is the permittivity in vacuum, ε_r is the relative permittivity of TiO_2 (taken as 50),[33] k is the Boltzmann constant, and T is the absolute temperature, taken as 298 K. From this analysis, the values of V_{FB} and N_D were extracted. The depletion layer width was calculated to validate the employed model through the equation $w = \sqrt{\frac{2\varepsilon_0\varepsilon_r}{eN_D}\left(\phi_{SC} - \frac{kT}{e}\right)}$. Carrier diffusion length was calculated by $L_n = l\sqrt{\frac{R_{ct}}{R_{tr}}}$, where R_{ct} is the charge transfer resistance and R_{tr} is the transport resistance, both extracted from the EIS analysis.

■ ASSOCIATED CONTENT

⑤ Supporting Information

The Supporting Information is available free of charge on the ACS Publications website at DOI: 10.1021/acsomega.9b02297.

J−V curves for different Zr additions, Tauc plots, structural and compositional information from XRD, EDS, and TEM, equivalent circuit for impedance fitting, values of series resistance, calculation of the width of the depletion region, and calculation of the diffusion length (PDF)

■ AUTHOR INFORMATION

Corresponding Authors
*E-mail: amayouf@ksu.edu.sa (A.M.A.).
*E-mail: sjulia@uji.es (S.G.).
ORCID ⊙
Maged N. Shaddad: 0000-0002-9495-3093
Francisco Fabregat-Santiago: 0000-0002-7503-1245
Juan Bisquert: 0000-0003-4987-4887
Sixto Gimenez: 0000-0002-4522-3174

Author Contributions

§M.N.S. and D.C.-M. have equally contributed to this work.

Notes

The authors declare no competing financial interest.

■ ACKNOWLEDGMENTS

■ REFERENCES

(1) Feng, X.; Shankar, K.; Varghese, O. K.; Paulose, M.; Latempa, T. J.; Grimes, C. A. Vertically aligned single crystal TiO₂ nanowire arrays grown directly on transparent conducting oxide coated glass: synthesis details and applications. *Nano Lett.* **2008**, *8*, 3781−3786.

(2) Liu, J.; Cao, G.; Yang, Z.; Wang, D.; Dubois, D.; Zhou, X.; Graff, G. L.; Pederson, L. R.; Zhang, J.-G. Oriented nanostructures for energy conversion and storage. *ChemSusChem* **2008**, *1*, 676.

(3) Quan, X.; Yang, S.; Ruan, X.; Zhao, H. Preparation of titania nanotubes and their environmental applications as electrode. *Environ. Sci. Technol.* **2005**, *39*, 3770−3775.

(4) Li, S.; Qiu, J.; Ling, M.; Peng, F.; Wood, B.; Zhang, S. Photoelectrochemical characterization of hydrogenated TiO₂ nanotubes as photoanodes for sensing applications. *ACS Appl. Mater. Interfaces* **2013**, *5*, 11129−11135.

(5) Fabregat-Santiago, F.; Barea, E. M.; Bisquert, J.; Mor, G. K.; Shankar, K.; Grimes, C. A. High carrier density and capacitance in TiO₂ Nanotube arrays induced by electrochemical doping. *J. Am. Chem. Soc.* **2008**, *130*, 11312−11316.

(6) Li, T. C.; Góes, M. S.; Fabregat-Santiago, F.; Bisquert, J.; Bueno, P. R.; Prasittichai, C.; Hupp, J. T.; Marks, T. J. Surface passivation of nanoporous TiO₂ via Atomic layer deposition of ZrO₂ for solid-state dye-sensitized solar cell Applications. *J. Phys. Chem. C* **2009**, *113*, 18385−18390.

(7) Ghori, M. Z.; Veziroglu, S.; Henkel, B.; Vahl, A.; Polonskyi, O.; Strunskus, T.; Faupel, F.; Aktas, O. C. A comparative study of photocatalysis on highly active columnar TiO₂ nanostructures in-air and in-solution. *Sol. Energy Mater. Sol. Cells* **2018**, *178*, 170−178.

(8) Wang, Y.; Li, H.; Chen, G.; Wang, Z.; Sang, Y.; Liu, H. PdO/TiO₂ nanobelt heterostructures with high photocatalytic activities based on an exposed highly active facet on ultrathin TiO₂ nanobelts. *Sol. Energy Mater. Sol. Cells* **2017**, *161*, 297−304.

(9) Yu, X.; Ren, N.; Qiu, J.; Sun, D.; Li, L.; Liu, H. Killing two birds with one stone: To eliminate the toxicity and enhance the photocatalytic property of CdS nanobelts by assembling ultrafine TiO₂ nanowires on them. *Sol. Energy Mater. Sol. Cells* **2018**, *183*, 41−47.

(10) Khan, S. U. M.; Al-Shahry, M.; Ingler, W. B., Jr. Efficient photochemical water splitting by a chemically modified n-TiO₂. *Science* **2002**, *297*, 2243−2245.

(11) Wang, G.; Wang, H.; Ling, Y.; Tang, Y.; Yang, X.; Fitzmorris, R. C.; Wang, C.; Zhang, J. Z.; Li, Y. Hydrogen-treated TiO₂ nanowire arrays for photoelectrochemical water splitting. *Nano Lett.* **2011**, *11*, 3026−3033.

(12) Pesci, F. M.; Wang, G.; Klug, D. R.; Li, Y.; Cowan, A. J. Efficient suppression of electron−hole recombination in oxygen-deficient hydrogen-treated TiO2Nanowires for photoelectrochemical water splitting. *J. Phys. Chem. C* **2013**, *117*, 25837−25844.

(13) Zhang, K.; Ravishankar, S.; Ma, M.; Veerappan, G.; Bisquert, J.; Fabregat-Santiago, F.; Park, J. H. Overcoming charge collection limitation at solid/liquid interface by a controllable crystal deficient overlayer. *Adv. Energy Mater.* **2017**, *7*, 1600923.

(14) Chen, X.; Liu, L.; Yu, P. Y.; Mao, S. S. Increasing solar absorption for photocatalysis with black hydrogenated titanium dioxide nanocrystals. *Science* **2011**, *331*, 746−750.

(15) Zhou, W.; Li, W.; Wang, J.-Q.; Qu, Y.; Yang, Y.; Xie, Y.; Zhang, K.; Wang, L.; Fu, H.; Zhao, D. Ordered Mesoporous Black TiO₂ as Highly efficient hydrogen evolution photocatalyst. *J. Am. Chem. Soc.* **2014**, *136*, 9280−9283.

(16) Nagaoka, H.; Ma, F.; deQuilettes, D. W.; Vorpahl, S. M.; Glaz, M. S.; Colbert, A. E.; Ziffer, M. E.; Ginger, D. S. Zr Incorporation into TiO₂ electrodes reduces hysteresis and improves performance in hybrid perovskite solar cells while increasing carrier lifetimes. *J. Phys. Chem. Lett.* **2015**, *6*, 669−675.

(17) Vasilopoulou, M.; Georgiadou, D. G.; Soultati, A.; Boukos, N.; Gardelis, S.; Palilis, L. C.; Fakis, M.; Skoulatakis, G.; Kennou, S.; Botzakaki, M.; Georga, S.; Krontiras, C. A.; Auras, F.; Fattakhova-Rohlfing, D.; Bein, T.; Papadopoulos, T. A.; Davazoglou, D.; Argitis, P. Atomic-layer-deposited Aluminum and Zirconium oxides for surface passivation of TiO₂ in high-efficiency organic photovoltaics. *Adv. Energy Mater.* **2014**, *4*, 1400214.

(18) Zhang, Y.; Yin, H.; Wang, A.; Liu, C.; Yu, L.; Jiang, T.; Hang, Y. Evolution of zirconia coating layer on rutile TiO₂ surface and the pigmentary property. *J. Phys. Chem. Solids* **2010**, *71*, 1458−1466.

(19) Chang, S.-m.; Doong, R.-a. Characterization of Zr-doped TiO₂ nanocrystals prepared by a nonhydrolytic Sol−Gel Method at high temperatures. *J. Phys. Chem. B* **2006**, *110*, 20808−20814.

(20) Kang, Q.; Cao, J.; Zhang, Y.; Liu, L.; Xu, H.; Ye, J. Reduced TiO₂ nanotube arrays for photoelectrochemical water splitting. *J. Mater. Chem. A* **2013**, *1*, 5766−5774.

(21) Miyoshi, A.; Nishioka, S.; Maeda, K. Water splitting on rutile TiO₂-based photocatalysts. *Chem. − Eur. J.* **2018**, *24*, 18204−18219.

(22) Albu, S. P.; Ghicov, A.; Aldabergenova, S.; Drechsel, P.; LeClere, D.; Thompson, G. E.; Macak, J. M.; Schmuki, P. Formation of double-walled TiO₂ Nanotubes and robust anatase membranes. *Adv. Mater.* **2008**, *20*, 4135−4139.

(23) Djerdj, I.; Tonejc, A. M. Structural investigations of nanocrystalline TiO₂ samples. *J. Alloys Compd.* **2006**, *413*, 159−174.

(24) Simka, W.; Majewski, D.; Nawrat, G.; Krząkała, A.; Nieużyła, Ł.; Michalska, J. Electrodeposition of Zirconium from DMSO solution. *Arch. Metall. Mater.* **2014**, *59*, 565−568.

(25) Grunthaner, F. J.; Grunthaner, P. J.; Vasquez, R. P.; Lewis, B. F.; Maserjian, J.; Madhukar, A. Local atomic and electronic structure of oxide/GaAs and SiO₂/Si interfaces using high-resolution XPS. *J. Vac. Sci. Technol.* **1979**, *16*, 1443−1453.

(26) Vásquez, G. C.; Peche-Herrero, M. A.; Maestre, D.; Alemán, B.; Ramírez-Castellanos, J.; Cremades, A.; González-Calbet, J. M.; Piqueras, J. Influence of Fe and Al doping on the stabilization of

the anatase phase in TiO2nanoparticles. *J. Mater. Chem. C* **2014**, *2*, 10377−10385.

(27) Wang, J.; Yu, Y.; Li, S.; Guo, L.; Wang, E.; Cao, Y. Doping behavior of Zr^{4+} Ions in Zr^{4+}-Doped TiO_2 Nanoparticles. *J. Phys. Chem. C* **2013**, *117*, 27120−27126.

(28) Wang, M.; Ioccozia, J.; Sun, L.; Lin, C.; Lin, Z. Inorganic-modified semiconductor TiO_2 nanotube arrays for photocatalysis. *Energy Environ. Sci.* **2014**, *7*, 2182−2202.

(29) Lukáč, J.; Klementová, M.; Bezdička, P.; Bakardjieva, S.; Šubrt, J.; Szatmáry, L.; Bastl, Z.; Jirkovský, J. Influence of Zr as TiO_2 doping ion on photocatalytic degradation of 4-chlorophenol. *Appl. Catal., B* **2007**, *74*, 83−91.

(30) Cui, H.; Zhao, W.; Yang, C.; Yin, H.; Lin, T.; Shan, Y.; Xie, Y.; Gu, H.; Huang, F. Black TiO_2 nanotube arrays for high-efficiency photoelectrochemical water-splitting. *J. Mater. Chem. A* **2014**, *2*, 8612−8616.

(31) Fernández, I.; Cremades, A.; Piqueras, J. Cathodoluminescence study of defects in deformed (110) and (100) surfaces of TiO_2 single crystals. *Semicond. Sci. Technol.* **2005**, *20*, 239−243.

(32) Bisquert, J. *Nanostructured Energy Devices: Equilibrium Concepts and Kinetics*; CRC Press: Boca Raton, 2015; 309.

(33) Fabregat-Santiago, F.; Garcia-Belmonte, G.; Bisquert, J.; Bogdanoff, P.; Zaban, A. Mott-Schottky analysis of nanoporous semiconductor electrodes in dielectric state deposited on SnO_2 (F) conducting substrates. *J. Electrochem. Soc.* **2003**, *150*, E293−E298.